Materials Today Energy 5 (2017) 99–106

Contents lists available at ScienceDirect

Materials Today Energy

journal homepage: www.journals.elsevier.com/materials-today-energy/

Improved Na-storage cycling of amorphous-carbon-sheathed Ni_3S_2 arrays and investigation by in situ TEM characterization

Xueke Xia [a, 1], Qiannan Wang [a, b, 1], Qi Zhu [a, b, 1], Jian Xie [a, c, *], Jiangwei Wang [a, b, **], Dagao Zhuang [d], Shichao Zhang [e], Gaoshao Cao [a], Xinbing Zhao [a, c]

[a] State Key Laboratory of Silicon Materials and School of Materials Science and Engineering, Zhejiang University, Hangzhou 310027, China
[b] Center of Electron Microscopy and School of Materials Science and Engineering, Zhejiang University, Hangzhou 310027, China
[c] Key Laboratory of Advanced Materials and Applications for Batteries of Zhejiang Province, Hangzhou 310027, China
[d] Dynabat New Energy Science & Technology Co., Ltd., Zhaoan 363500, China
[e] School of Materials Science and Engineering, Beijing University of Aeronautics and Astronautics, Beijing 100191, China

ARTICLE INFO

Article history:
Received 9 March 2017
Received in revised form
26 April 2017
Accepted 14 May 2017

Keywords:
Nickel sulfide
Amorphous carbon sheath
Array electrode
Sodium ion battery
In situ transmission electron microscopy

ABSTRACT

The past few years have witnessed increasing attention of sodium ion batteries due to the concerns on the shortage of lithium resources. Great challenge, however, remains to develop anode materials with high capacity and long cycle life. In this work, a binder-free array-type electrode, constructed of nickel sulfide (Ni_3S_2) nanoparticles encapsulated in amorphous carbon sheath (ACS), was fabricated by a facile templating method. This array-type Ni_3S_2/ACS electrode can yield a high initial reversible capacity of 772 mAh g^{-1} and a long cycle life with a reversible capacity of 440 mAh g^{-1} retained after 100 cycles. Both ex situ and in situ characterizations reveal that the excellent electrochemical performance of Ni_3S_2/ACS electrode originates from the unique array-type structure, in which high activity of Ni_3S_2 can be obtained by the thin-layered structure and the sodiation-induced volume expansion of Ni_3S_2 can be effectively accommodated by the carbon sheath and inner space, resulting in a high mechanical stability of the Ni_3S_2/ACS rods during cycling. Our results reveal the electrochemical performance and fundamental reaction mechanism of Ni_3S_2/ACS during sodiation-desodiation cycles, shedding lights onto the design of novel sulfide-based anodes for sodium ion batteries.

1. Introduction

Modern society has witnessed the ever increasing applications of Li-ion batteries (LIBs) in portable electronic devices (e.g. smart phone, laptop, and digital camera) and electric vehicles (EV), to reduce the dependence on fossil fuels and greenhouse gas emission [1–4]. The shortage of lithium reserves and currently immature battery recycling technology, however, cause a serious concern about the sustainable application of LIBs in near future [5–7]. As a consequence, batteries based on the alkali metals with abundant resources and low costs, such as Na-ion batteries (NIBs), have grained more and more attentions during past few years [6–12]. NIBs show potential applications in electrical energy storage for grid, solar cells and wind turbines, where the energy density is not a concern [11,13,14]. A critical problem of NIBs is the low electrochemical activity compared with LIBs [15], which is ascribed to the large radius of sodium ions, resulting in its difficulty to insert into the intercalation-type anodes, such as the widely-used graphitized carbon materials in commercial LIBs [16,17]. Inspired by the knowledge of LIBs, alloying and conversion type electrodes may be a potential solution to overcome this challenge in NIBs. For the alloying mechanism, recent studies have showed that sodium can reversibly alloy/dealloy with some metals and alloys (e.g. Sb, Sn, hollow NiSb and Sn-P-based composite, etc) to deliver high capacity and good cycling stability [18–27].

Among the conversion-type anodes, previous studies mainly focused on the transition metal oxides [25,27], which delivered high Na-storage capacity but still suffered from low Na-storage activity. Recently, sulfides, such as FeS_2 [28], FeS [29], CoS_2 [30], Co_9S_8 [31], MoS_2 [32–34], WS_2 [35,36], and Ni_3S_2 [37,38], were

---

* Corresponding author. School of Materials Science and Engineering, Zhejiang University, Hangzhou 310027, China.

** Corresponding author. School of Materials Science and Engineering, Zhejiang University, Hangzhou 310027, China.

E-mail addresses: xiejian1977@zju.edu.cn (J. Xie), jiangwei_wang@zju.edu.cn (J. Wang).

[1] Xueke Xia, Qiannan Wang, and Qi Zhu contributed equally to this work.

http://dx.doi.org/10.1016/j.mtener.2017.05.003

found to demonstrate high Na-storage activities, along with other advantages including low cost, environmental friendliness and easy preparation. Nevertheless, rapid capacity fade often occurred during the application of these conversion-type sulfide anodes in NIBs owing to the large volume changes upon sodiation/desodiation. Further engineering the sulfides with flexible matrix, such as graphene nanosheets (GNS) and carbon nanofibers (CNF), were further employed to alleviate the electrochemical degradation and thereby capacity fade of sulfide anodes [39,40]. For example, a MoS_2/GNS hybrid could deliver an initial capacity of 573 mAh g^{-1} at 200 mA g^{-1} and maintain a capacity of 322 mAh g^{-1} after 600 cycles at 1.3 A g^{-1} [33]; while the Sb nanoparticles encapsulated in macroporous carbon could keep 93% of its initial capacity after 500 cycles [41]. As a typical sulfide, the electrochemical performance of Ni_3S_2 anode in NIBs, however, remains unsatisfactory yet [37,38,42].

In this work, we designed a binder-free array-type electrode by a simple templating method. In this electrode, Ni_3S_2 were directly grew and encapsulated inside amorphous carbon sheath (ACS), forming three-dimensional (3D) hollow-structural Ni_3S_2/ACS arrays on Ni foam substrate. In situ transmission electron microscopy (TEM) electrochemical testing revealed that the volume expansion of Ni_3S_2 during the sodiation process can be effectively buffered by the voids inside the ACS, and the structural integrity of the Ni_3S_2/ACS rods can be kept by the carbon sheath after electrochemical cycling. As a result, the Ni_3S_2/ACS arrays exhibited a high initial capacity of 722 mAh g^{-1} at 50 mA g^{-1} and a long cycle life with a capacity of 440 mAh g^{-1} retained after 100 cycles.

2. Experimental section

2.1. Preparation of ZnO nanorods (NRs) on Ni substrate

The ZnO NRs were synthesized on Ni substrate by a facile hydrothermal route. In a typical synthesis, $Zn(NO_3)_2 \cdot 6H_2O$ (268 mg) and methenamine (127 mg) were dissolved in 30 mL of deionized (DI) water with magnetic stirring for 10 min to form a uniform solution. Then, 2.4 mL of ammonia water (25 wt%) was added to the above solution with stirring for 15 min to obtain a transparent solution. A piece of Ni foam (1.6 cm × 4.8 cm) was immersed in a $KMnO_4$ aqueous solution (0.5 mol L^{-1}) for 1 h and rinsed with DI water sufficiently, which was then steeped in the above transparent solution for 10 h. After that, the solution with Ni foam was transferred into a 50 mL Teflon-lined stainless steel autoclave and held at 90 °C for 24 h in an electric oven before cooling down to room temperature. The Ni-supported ZnO was finally obtained by rinsing with DI water and absolute ethanol several times followed by heating at 60 °C in air overnight.

2.2. Preparation of Ni-supported Ni_3S_2/ACS

The Ni-supported ZnO NRs were used as templates to grow Ni-supported Ni_3S_2/ACS. First, a solution for Ni_3S_2 growth was prepared by mixing 30 mg of thioacetamide and 142 mg of Na_2SO_4 in 35 mL of DI water under stirring for 30 min. The solution was then transferred into a 50 mL Teflon-lined stainless steel autoclave with the Ni-supported ZnO immersed. The autoclave was heated in an electric oven at 120 °C for 3 h followed by cooling to room temperature. The Ni foam with deposit was collected from the autoclave, washed with DI water and absolute ethanol several times, and heated at 60 °C in air overnight to obtain Ni-supported ZnO/Ni_3S_2. Carbon coating on ZnO/Ni_3S_2 was conducted by immersing the Ni-supported ZnO/Ni_3S_2 in an aqueous solution of glucose (0.06 mol L^{-1}) overnight followed by firing at 500 °C in Ar for 3 h. The final product, Ni-supported Ni_3S_2/ACS was obtained by immersing the above product in an aqueous solution of NaOH (1.5 mol L^{-1}) for 48 h to remove ZnO. The preparation procedure of the Ni-supported Ni_3S_2/ACS is schematically illustrated in Fig. 1a. The electronic conductivity of the pyrolytic carbon from glucose and graphite was measured on a custom designed apparatus using a DC four-probe method.

2.3. Structural characterization

X-ray diffraction (XRD) patterns of the electrodes were collected on a Rigaku D/Max-2550pc powder diffractometer equipped with monochromatized Cu K_α radiation ($\lambda = 1.541$ Å). Morphologies of the original and cycled electrodes were characterized by field-emission scanning electron microscopy (SEM) on an S-4800 microscope (Hitachi, Japan). The microstructures of the materials from the pristine and sodiated/desodiated electrodes were analyzed by TEM and High-resolution TEM (HRTEM) on a JEM 2100F microscope. For the post-mortem SEM and TEM characterizations, the electrodes or electrode components were carefully handled to minimize the exposure to air according to our previous report [43].

2.4. Electrochemical measurements

CR2025 coin cells were fabricated in an Ar-filled glove box with Na foils as counter electrodes, Ni_3S_2/ACS arrays on Ni substrate as working electrodes, and glass fiber (Whatman GF/D) as separators. Before cells fabrication, the working electrodes were dried at 110 °C in vacuum overnight. The electrolyte used was 1 M $NaPF_6$ in ethylene carbonate (EC)/diethyl carbonate (DEC) (1:1 in volume). Fluoroethylene carbonate (FEC) was used as electrolyte additive with a FEC/EC + DEC volume ratio of 5%. Cyclic voltammetry (CV) scanning was carried out on a VersaSTAT3 electrochemistry workstation (Princeton Applied Research) over a voltage range of 0.005–3 V (vs. Na/Na^+) at 0.1 mV s^{-1}. Galvanostatic cycling was conducted on a Neware battery cycler (Shenzhen, China) between 0.005 and 3.0 V (vs. Na/Na^+) at various current densities. All of the electrochemical measurements were performed at 25 °C.

2.5. In situ TEM characterization

In situ TEM characterization was performed on a FEI Tecnai F20 TEM using the Nanofactory TEM-scanning tunneling microscopy (STM) holder. The configuration of the device for in situ characterization is shown in Fig. S1. Typically, a nanosized Na cell was assembled to study the sodiation/desodiation mechanisms of Ni_3S_2/ACS electrodes. The nanosized NIB cell consisted of a working electrode of Ni_3S_2/ACS nanorods on a Pt rod, a counter electrode of metallic sodium on a W rod, and a solid electrolyte of Na_2O + NaOH formed naturally on the surface of Na metal [44,45]. After the contact between solid electrolyte and Ni_3S_2/ACS was established, a potential of −1 V was applied to the Ni_3S_2/ACS to initiate the sodiation and +6–8 V for the desodiation. Both beam-on and beam-off experiments were carried out to exclude the beam irradiation on the alloying/dealloying processes.

3. Results and discussion

Fig. 1a shows the preparation procedure of Ni-supported Ni_3S_2/ACS arrays using Ni-supported ZnO NRs as the templates. In the as-fabricated products, Ni_3S_2 is expected to be encapsulated in the carbon sheath. Fig. 1b and c show that ZnO NRs obtained by the hydrothermal reaction had a length of around 2–4 μm and were uniformly distributed on the skeleton of Ni foam substrate (Ni + ZnO). The porous structure of Ni foam was maintained, favoring the electrolyte wetting of electrode. After Ni_3S_2 deposition,

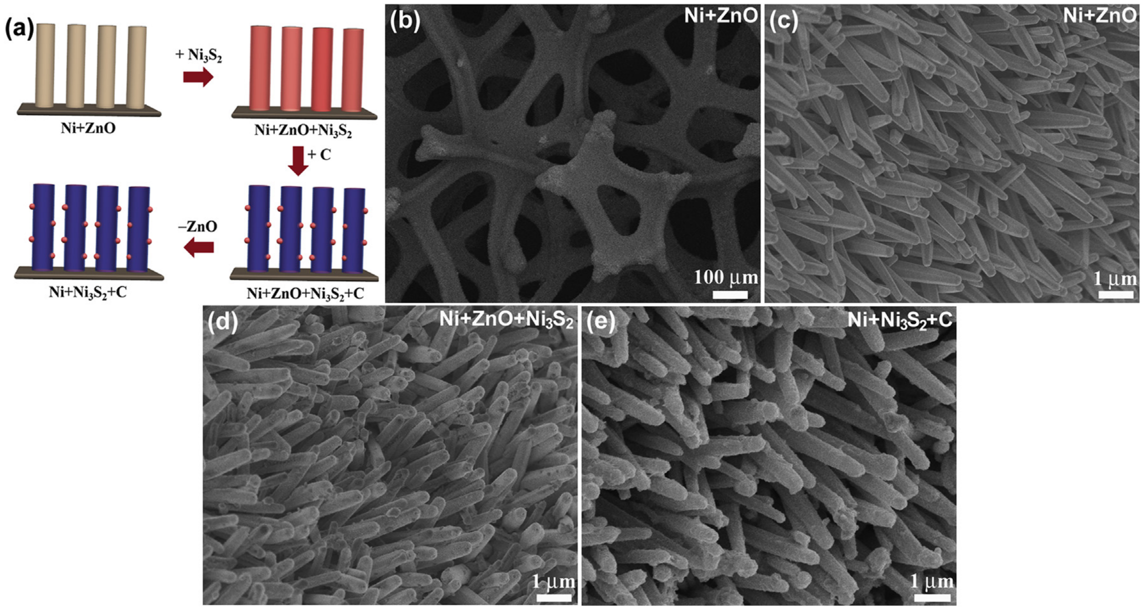

Fig. 1. (a) Schematic illustration of the synthetic route and (b–e) SEM images of the products at different synthetic stages.

no obvious morphology change occurred, indicating a conformal growth of Ni_3S_2 on the surface of ZnO NRs (Ni + ZnO + Ni_3S_2, Fig. 1d). Ni-supported Ni_3S_2/ACS (Ni + Ni_3S_2+C) arrays were then obtained by depositing carbon on Ni + ZnO + Ni_3S_2 and subsequently removing ZnO NRs with NaOH etching, during which the array-type structure was well preserved but the surface roughness of Ni_3S_2/ACS arrays increased greatly compared with the pristine ZnO NRs (Fig. 1e). XRD patterns in Fig. 2 verify the successive formations of ZnO and Ni_3S_2 during the fabrication of Ni-supported Ni_3S_2/ACS. No ZnO peak existed in the final products of Ni + Ni_3S_2+C, indicating the complete removal of ZnO after the etching. Raman spectrum in Supporting Information Fig. S2 confirms the presence of carbon in the final products, but it should be in the amorphous state due to the lack of crystalline carbon peaks in the XRD diffraction of Ni + Ni_3S_2+C.

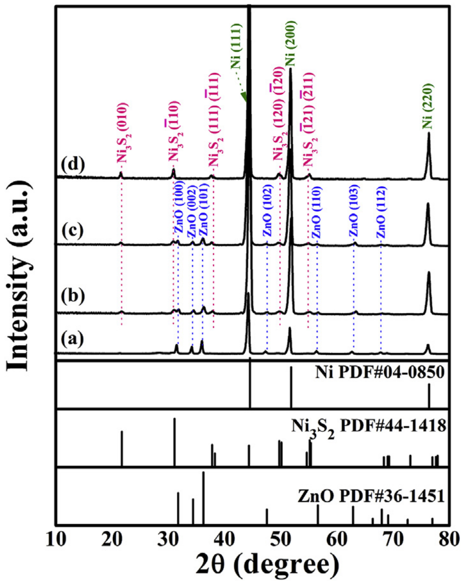

Fig. 2. XRD patterns of the products at different synthetic stages with final product Ni-supported Ni_3S_2/ACS: (a) Ni + ZnO, (b) Ni + ZnO + Ni_3S_2, (c) Ni + ZnO + Ni_3S_2+C, and (d) Ni + Ni_3S_2+C.

TEM analysis was further conducted to characterize the microstructure of Ni_3S_2/ACS rods. Fig. 3a shows that the wall of each Ni_3S_2/ACS rod has a bilayer structure, with the thicknesses of 40–60 and 30–40 nm for the outer (light contrast) and inner layers (dark contrast), respectively, as demonstrated by the magnified view in Fig. 3b. According to the preparation procedure, the outer and inner layers of the wall should be carbon and Ni_3S_2, respectively, as verified by the high-angle annular dark-field (HAADF)-scanning transmission electron microscopy (STEM) images and the corresponding energy dispersive X-ray spectrometry (EDX) mapping in Fig. 3c–j. Clearly, the Ni_3S_2/ACS anode has a bilayer structure with the inner layer of Ni_3S_2 and the outer layer of amorphous carbon (Fig. 3c–j). It is noted that the Ni and S elements also showed up in the carbon layer, as indicated by the superimposed EDS mapping in Fig. 3h–j. This should be induced by the diffusion of Ni and S during the pyrolysis treatment under high temperature, resulting in numerous Ni_3S_2 nanoparticles on the surface of carbon layer, as demonstrated by Fig. S3.

Electrochemical sodiation/desodiation mechanism of the Ni-supported Ni_3S_2/ACS was investigated by CV scanning. Fig. 4a presents the first five cycles of CV plots swept at 0.1 mV s^{-1} in the voltage window of 0.005 and 3.0 V. During the first scan, there is a sharp reduction peak between 0 and 0.5 V, which can be attributed to the electrolyte decomposition reaction and the conversion reaction $4Na^+ + 4e^- + Ni_3S_2 \rightarrow 3Ni + 2Na_2S$ [37]. In the second scan, two reduction peaks appear between 0.5 and 1.0 V, suggesting different reactions occurred as compared with the first cycle. In the first anodic scan, the sharp peak at around 2.0 V is assigned to the decomposition of Na_2S ($Na_2S \rightarrow S + 2Na^+ + 2e^-$). During the subsequent scans, the anodic peaks are almost overlapped, indicative reversible reactions. However, it is yet unclear that whether the Ni_3S_2 crystal lattice can be recovered after charge, which will be clarified by the in situ TEM characterization as discussed below. The electrochemical Na-storage performance of the Ni-supported Ni_3S_2/ACS was evaluated by galvanostatic cycling at 50 mA g^{-1} between 0.005 and 3.0 V, with the initial three charge/discharge cycles shown in Fig. 4b. The electrode delivers the first discharge

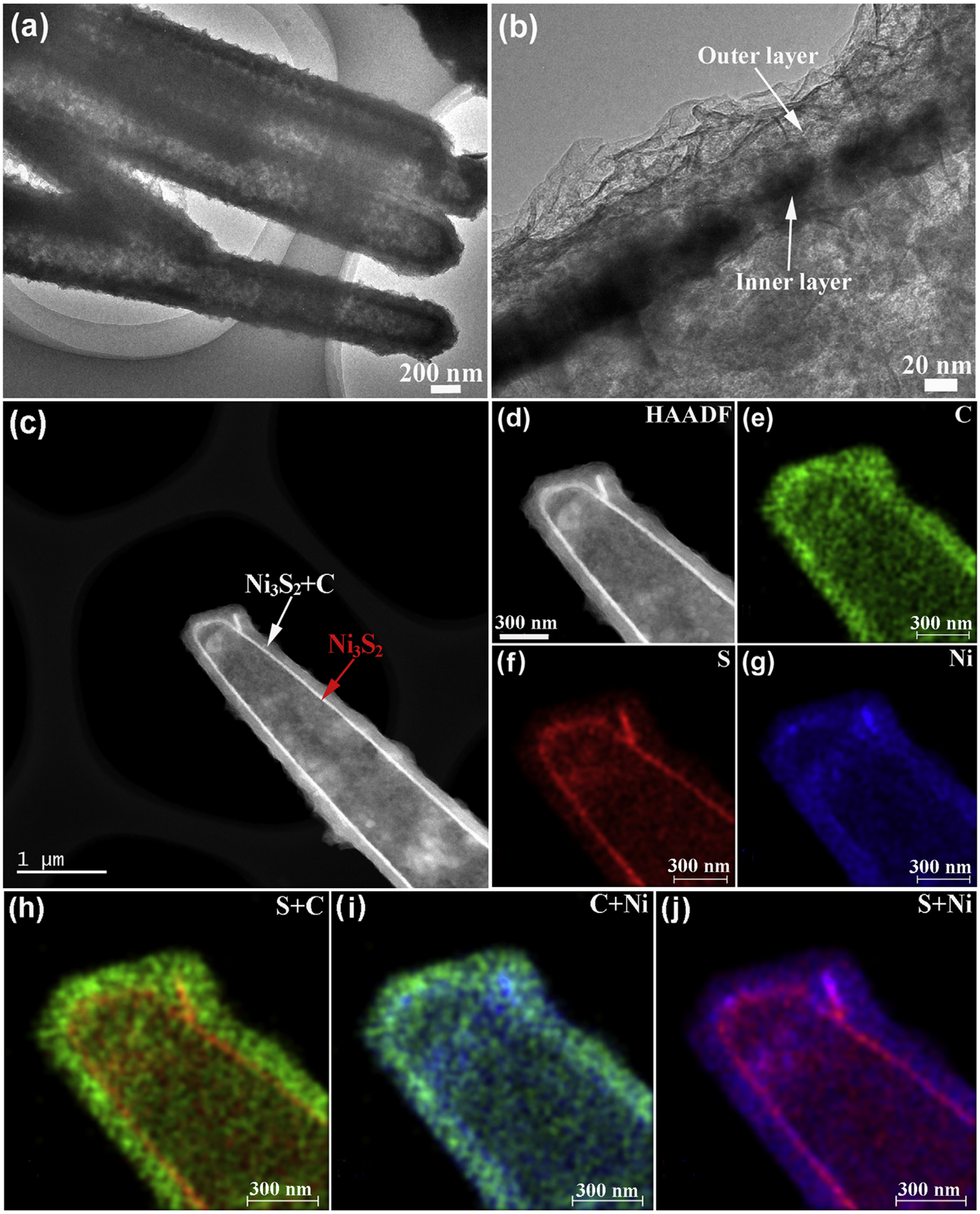

Fig. 3. (a, b) TEM images, (c–g) HAADF-STEM image and EDS mapping of Ni_3S_2/ACS, and (h–j) superimposed EDS mapping.

(sodiation) and charge (desodiation) capacities of 1193 and 772 mAh g^{-1}, respectively, which are higher than those in the previous reports [37,38,42]. The higher electrochemical activity of Ni_3S_2/ACS may be due to such factors as array-type structure that facilitates electrode wetting, small size of the Ni_3S_2 particles and good contact between amorphous carbon and Ni_3S_2. Fig. 4c shows the cycling performance of the Ni-supported Ni_3S_2/ACS electrode at 50 mA g^{-1}. It can be seen that the electrode shows relatively stable cycling after initial relatively rapid capacity fade. After 100 cycles, Ni_3S_2/ACS can maintain a high charge capacity of 440 mAh g^{-1}, which is higher than those of the carbon-based materials [16]. The electronic conductivity of the carbon pyrolyzed from glucose at 1000 °C is only 0.26 S cm^{-1} at room temperature, much lower than that of the graphite (210 S cm^{-1} at room temperature). Therefore, ACS may only act as the substrate to support Ni_3S_2 after ZnO etching and contributes little to the improvement of the electronic conductivity. Actually, the rate performance of Ni_3S_2/ACS electrode is not satisfactory (Fig. S4a). We compared the electrochemical performance between Ni_3S_2/ACS arrays and the Ni_3S_2 particles grown directly on Ni foam. It can be seen that with the supporting and

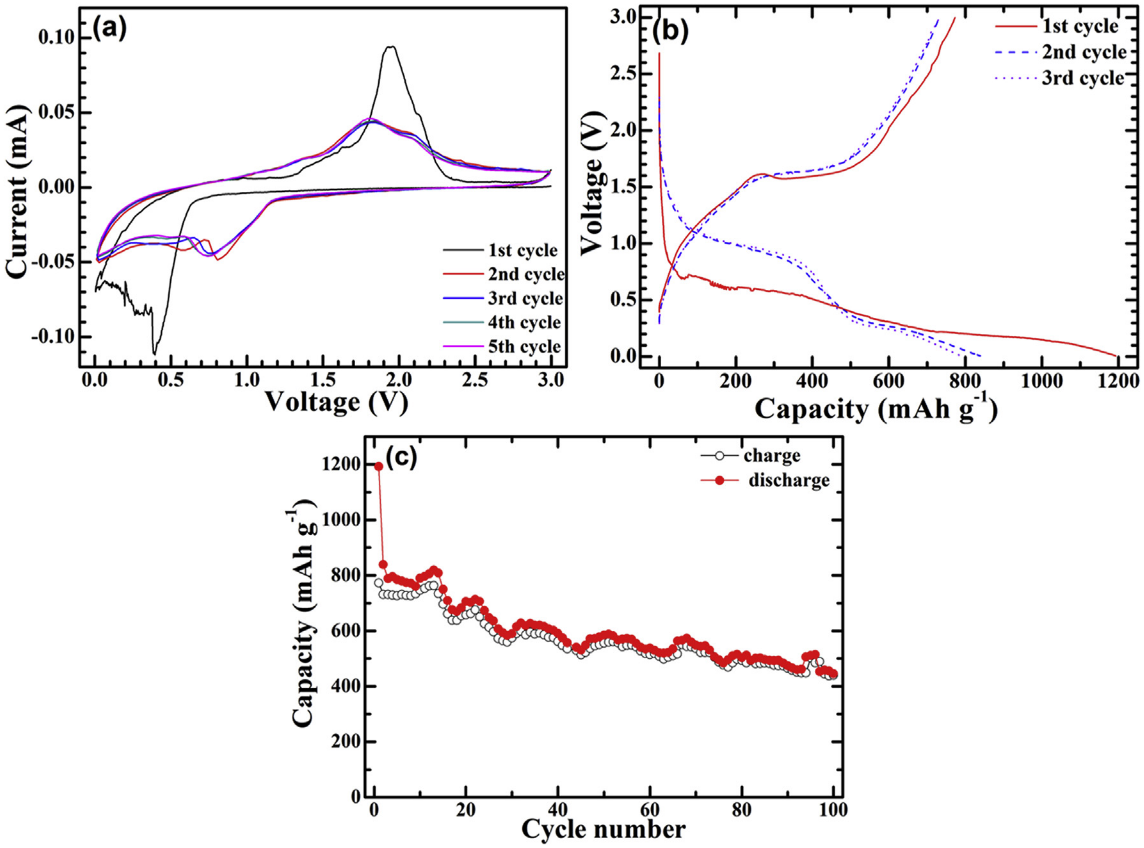

Fig. 4. (a) CV plots, (b) voltage profiles and (c) cycling stability of Ni_3S_2/ACS at 50 mA g^{-1}.

dispersing effect of ACS, the Ni_3S_2/ACS shows a higher reversible capacity and improved cycling performance (Fig. S4b).

Ex-situ and in situ characterizations were conducted to understand the good cycling stability of Ni_3S_2/ACS. SEM image in Fig. 5a shows that the array-type structure of Ni-supported Ni_3S_2/ACS electrode is well kept after discharge, indicating its mechanical robustness during cycling; however, the surface roughness of the discharged rods increases significantly due to the formation of solid electrolyte interface (SEI) layers on the outer surface. TEM image in Fig. 5b displays that the bilayer structure of Ni_3S_2/ACS is well preserved and the Ni_3S_2 remains confined inside the carbon sheath after sodiation, suggesting the robust behavior of the Ni_3S_2/ACS array upon the reversible volume changes. Selected area electron diffraction (SAED) pattern in Fig. 5c shows that the sodiation product is Na_2S and Ni, consistent with the CV measurement. The SAED pattern also indicates that there is residual Ni_3S_2 in the sodiation product. After desodiation, no fracture or pulverization occurs in this array-type Ni_3S_2/ACS after reversible volume changes (Fig. 5d).

Movies have been captured to show the dynamic structural changes of Ni_3S_2/ACS. Fig. 6 and Movie S1 present the dynamic structural changes of an individual Ni_3S_2/ACS anode upon sodiation and desodiation. The pristine Ni_3S_2/ACS rod consists of the inner layer of Ni_3S_2 (dark contrast) and the outer layer of carbon (light contrast), with a taper structure along the axial direction. A small Ni_3S_2 nanoparticle (with the diameter of 180 nm) is attached onto the surface of this Ni_3S_2/ACS rod (pointed out by the black arrow in Fig. 6a), enabling a direction comparison between the sodiation/desodiation behavior of bare Ni_3S_2 and Ni_3S_2/ACS anodes. Fig. 6a–f demonstrate that this Ni_3S_2/ACS rod shows a robust behavior in one sodiation/desodiation cycle, consistent with the ex situ observation presented in Fig. 5. Upon sodiation, we observe that the volume expansion of the inner Ni_3S_2 layer can be completely accommodated by the amorphous carbon without any structural damage due to the mechanical confinement and buffering effect of surface carbon layer [46], though the sodiation-induced diameter increase of Ni_3S_2/ACS rod still occurs because of the sodiation-induced large hoop strains that results in outward radial displacement [46]. After full reaction, the diameter of this Ni_3S_2/ACS rod increases from 751 nm to 815 nm with negligible axial elongation, corresponding to a radial expansion of ~8.5% (Due to overlapping with the other sample, the changes of inner diameter of this Ni_3S_2/ACS rod cannot be clearly identified). In strong contrast, without the protection of carbon coating, a large crack appears on the bare Ni_3S_2 nanoparticle upon the initial sodiation (pointed out by the red arrow in Fig. 6b). Such sodiation-induced crack could result in the pulverization and thereby capacity fading of pure Ni_3S_2 anode. It should be mentioned that a large particle with the diameter of 500 nm is formed the surface of ACS sheath after 70 s sodiation (pointed out by the black arrow in Fig. 6c), which is the Na dendrite nucleated during sodiation via the fast surface diffusion under the high potential. Similar phenomenon was observed in other in situ TEM studies of other anodes for sodium-ion batteries, such as Sn nanoparticle [47], which should be avoided in real batteries. After full sodiation, the pristine Ni_3S_2 phase is transformed to Na_2S and Ni phases (identified by the SAED patterns in Fig. 6g and h), confirming the conversion reaction of $4Na^+ + 4e^- + Ni_3S_2 \rightarrow 3Ni + 2Na_2S$ [37]. Note that some sodium dendrites also form on the surface of sodiated sample due to the overcharge (pointed out by the black arrow in Fig. 6c), which will shrink and eventually disappear with the extraction of sodium ions. In the following desodiation, the sodiation product of Na_2S is gradually transformed

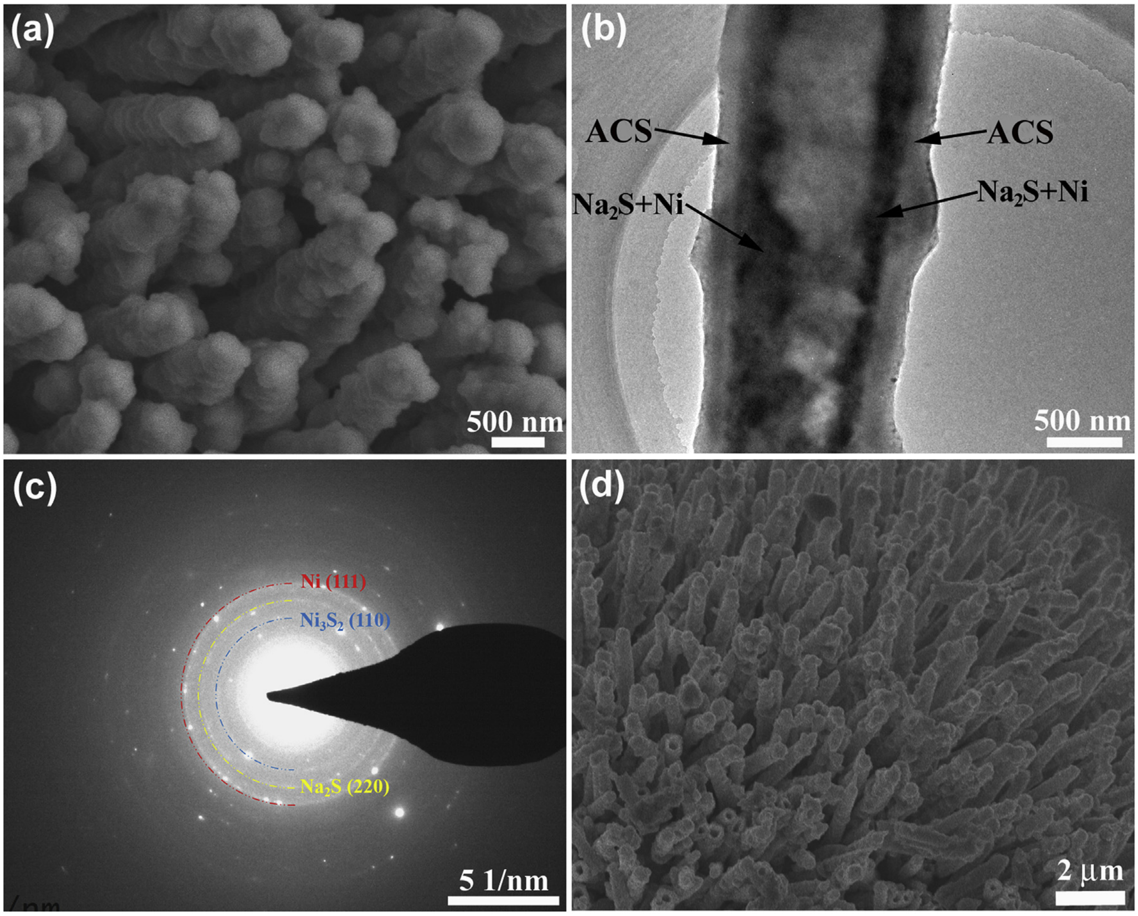

Fig. 5. (a) SEM image, (b) TEM image and SAED patterns of Ni_3S_2/ACS after the first discharge, and (d) SEM image of Ni_3S_2/ACS after the first charge.

back to S, causing diameter shrinkage of the sodiated rod (Fig. 6d–f and Movie S2). SAED pattern in Fig. 6i indicates that the desodiation products are S and Ni, suggesting that the recovery of the Ni_3S_2 lattice cannot be achieved. In other words, the capacity comes from the reversible sodiation/desodiation of element S in Ni matrix. The total reaction mechanism can be written as:

$$4Na^+ + 4e^- + Ni_3S_2 \rightarrow 3Ni + 2Na_2S \quad (1)$$

$$2Na_2S + 3Ni \leftrightarrow 2S + 3Ni + 4Na^+ + 4e^- \quad (2)$$

The reaction mechanism of the Ni_3S_2/ACS arrays is also schematically illustrated in Fig. S5.

Supplementary video related to this article can be found at http://dx.doi.org/10.1016/j.mtener.2017.05.003.

Fig. 7 and Movie S3 show the sodiation of another Ni_3S_2/ACS rod, in which the dynamic changes of the inner diameter can be clearly identified. Similar to the sample shown in Fig. 6, sodiation causes an outward expansion of the Ni_3S_2/ACS rod, with a radial expansion of 13.5% after full sodiation. More importantly, the sodiation also results in a decrease of the inner diameter from 524 nm to 495 nm, which can be attributed to the mechanical confinement of surface carbon layers on the inner Ni_3S_2 layer. Such inward expansion, to some extent, could alleviate the outward expansion-induced pulverization and thereby fracture of SEI layer formed on the outer surface of Ni_3S_2/ACS rod. As a result, high mechanical stability is obtained in our Ni-supported array-type Ni_3S_2/ACS electrode structure. However, it should be stated that the array-type Ni_3S_2/ACS electrode still shows capacity fade despite the robust structure of the Ni_3S_2/ACS rods. This may be caused by the dissolution of the polysulfides during cycling, similar to the case in Li–S batteries [48]. As shown in Fig. S6, numerous small particles form on the surface of sodiated Ni_3S_2/ACS rod, which are reaction products of surface Ni_3S_2 particles, i.e. Na_2S and Ni nanoparticles. In the subsequent cycling, their desodiation product of S can be dissolved into the electrolytes in real batteries, causing gradual capacity decay. Therefore, further work need to be conducted for optimizing the structure design of array-type Ni_3S_2/ACS electrodes to achieve an improved battery performance.

4. Conclusions

In summary, a binder-free array-type Ni_3S_2/ACS electrode was fabricated directly on Ni foam substrate by a facile route using ZnO NRs as the templates. The small size and intimate contact with amorphous carbon endow Ni_3S_2 with a high electrochemical Na-storage activity. The Ni_3S_2/ACS array electrode can deliver a high reversible capacity of 772 mAh g^{-1} at a current density of 50 mA g^{-1}. The volume expansion of Ni_3S_2 upon sodiation can be buffered by the carbon sheaths and inner space, leading to the structural robustness of the array-type electrode. As a result, the Ni_3S_2/ACS array electrode exhibits a long cycle life with a reversible capacity of 440 mAh g^{-1} retained after 100 cycles at 50 mA g^{-1}. This work provides a new design of anode for high-performance Na-ion batteries.

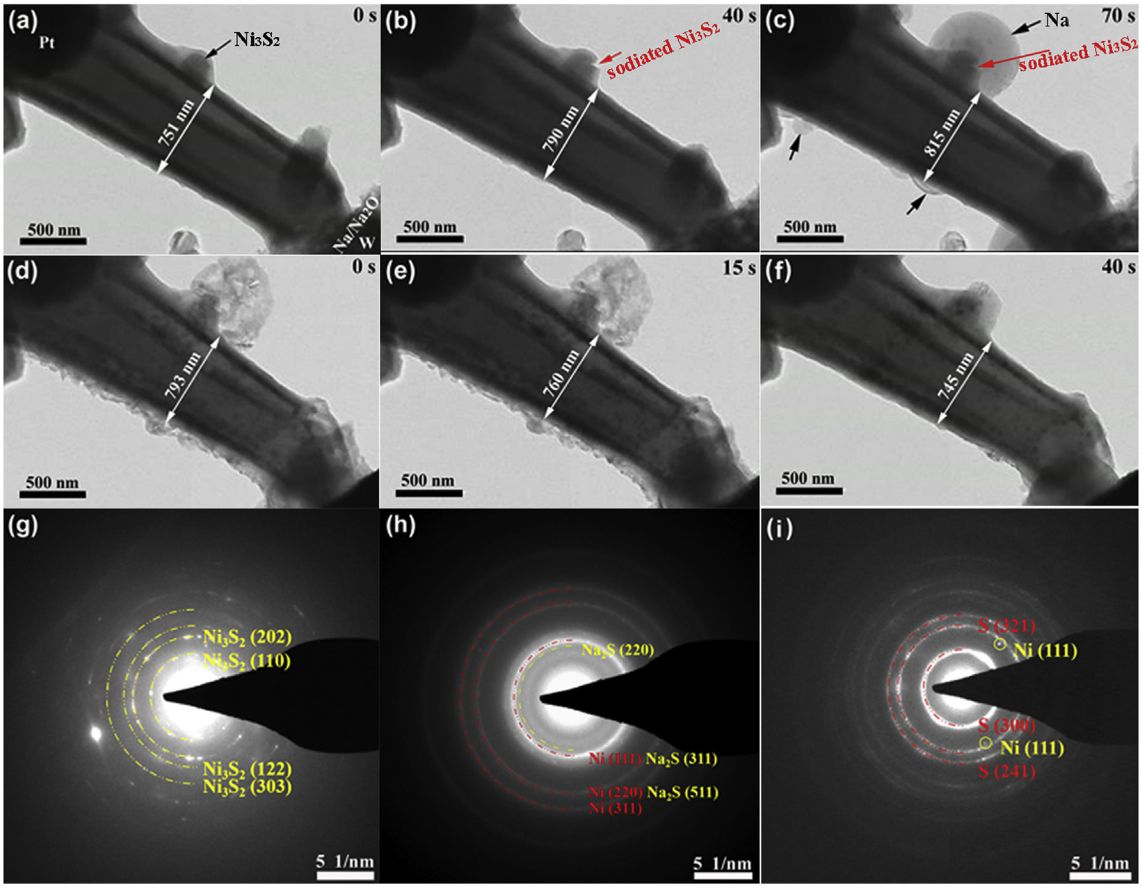

Fig. 6. Dynamic processes of (a–c) sodiation and (d–f) desodiation of a Ni_3S_2/ACS rod, and SAED patterns of the (g) pristine, (h) sodiated and (i) desodiated Ni_3S_2/ACS.

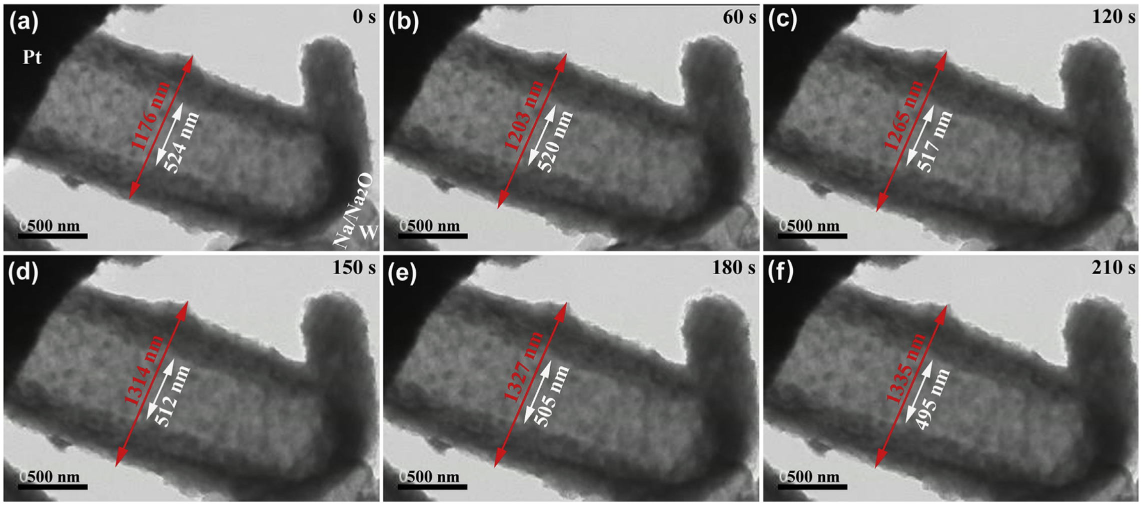

Fig. 7. Dynamic sodiation process of a thicker Ni_3S_2/ACS rod.

Acknowledgements

This work was supported by the National Basic Research Program of China (2013CB934001), the National Natural Science Foundation of China (No. 51572238), Zhejiang Provincial Natural Science Foundation of China under Grant No. LY15E010004, Development and Application for Sodium Ion battery (2016GK4030), and Program for Innovative Research Team in University of Ministry of Education of China (IRT13037). J.W. acknowledges the support of the Chinese 1000-Youth-Talent Plan.

Appendix A. Supplementary data

Supplementary data related to this article can be found at http://dx.doi.org/10.1016/j.mtener.2017.05.003.

References

[1] U. Eberle, R. von Helmolt, Sustainable transportation based on electric vehicle concepts: a brief overview, Energy Environ. Sci. 3 (2010) 689–699.

[2] V. Etacheri, R. Marom, R. Elazari, G. Salitra, D. Aurbach, Challenges in the development of advanced Li-ion batteries: a review, Energy Environ. Sci. 4 (2011) 3243–3262.

[3] M.M. Thackeray, C. Wolverton, E.D. Isaacs, Electrical energy storage for transportation–approaching the limits of, and going beyond, lithium-ion batteries, Energy Environ. Sci. 5 (2012) 7854–7863.

[4] J.B. Dunn, L. Gaines, J.C. Kelly, C. James, K.G. Gallagherc, The significance of Li-ion batteries in electric vehicle life-cycle energy and emissions and recycling's role in its reduction, Energy Environ. Sci. 8 (2015) 158–168.

[5] J.M. Tarascon, Is lithium the new gold? Nat. Chem. 2 (2012) 510, 510.

[6] S.W. Kim, D.H. Seo, X.H. Ma, G. Ceder, K. Kang, Electrode materials for rechargeable sodium-ion batteries: potential alternatives to current lithium-ion batteries, Adv. Energy Mater. 2 (2012) 710–721.

[7] M.D. Slater, D. Kim, E. Lee, C.S. Johnson, Sodium-ion batteries, Adv. Funct. Mater. 23 (2013) 947–958.

[8] V. Palomares, P. Serras, I. Villaluenga, K.B. Hueso, J. Carretero González, T. Rojo, Na-ion batteries: recent advances and present challenges to become low cost energy storage systems, Energy Environ. Sci. 5 (2012) 5884–5901.

[9] V. Palomares, M. Casas Cabanas, E. Castillo Martínez, M.H. Han, T. Rojo, Update on Na-based battery materials. A growing research path, Energy Environ. Sci. 6 (2013) 2312–2337.

[10] N. Yabuuchi, K. Kubota, M. Dahbi, S. Komaba, Research development on sodium-ion batteries, Chem. Rev. 114 (2014) 11636–11682.

[11] D. Kundu, E. Talaie, V. Duffort, L.F. Nazar, The emerging chemistry of sodium ion batteries for electrochemical energy storage, Angew. Chem. Int. Ed. 54 (2015) 3431–3448.

[12] L.P. Wang, L.H. Yu, X. Wang, M. Srinivasan, Z.J. Xu, Recent developments in electrode materials for sodium-ion batteries, J. Mater. Chem. A 3 (2015) 9353–9378.

[13] B. Dunn, H. Kamath, J.M. Tarascon, Electrical energy storage for the grid: a battery of choices, Science 334 (2011) 928–935.

[14] M. Sawicki, L.L. Shaw, Advances and challenges of sodium ion batteries as post lithium ion batteries, RSC Adv. 5 (2015) 53129–53154.

[15] S.Y. Hong, Y. Kim, Y. Park, A. Choi, N.S. Choi, K.T. Lee, Charge carriers in rechargeable batteries: Na ions vs. Li ions, Energy Environ. Sci. 6 (2013) 2067–2081.

[16] M.M. Doeff, Y.P. Ma, S.J. Visco, L.C. De Jonghe, Electrochemical insertion of sodium into carbon, J. Electrochem. Soc. 140 (1993) L169–L170.

[17] R. Alcántara, F.J.F. Madrigal, P. Lavela, J.L. Tirado, J.M.J. Mateos, C.G. de Salazar, R. Stoyanova, E. Zhecheva, Characterisation of mesocarbon microbeads (MCMB) as active electrode material in lithium and sodium cells, Carbon 38 (2000) 1031–1041.

[18] A. Darwiche, C. Marino, M.T. Sougrati, B. Fraisse, L. Stievano, L. Monconduit, Better cycling performances of bulk Sb in Na-ion batteries compared to Li-ion systems: an unexpected electrochemical mechanism, J. Am. Chem. Soc. 134 (2012) 20805–20811.

[19] L. Wu, X.H. Hu, J.F. Qian, F. Pei, F.Y. Wu, R.J. Mao, X.P. Ai, H.X. Yang, Y.L. Cao, Sb–C nanofibers with long cycle life as an anode material for high-performance sodium-ion batteries, Energy Environ. Sci. 7 (2014) 323–328.

[20] J. Liu, Z.Z. Yang, J.Q. Wang, L. Gu, J. Maier, Y. Yu, Three-dimensionally interconnected nickel–antimony intermetallic hollow nanospheres as anode material for high-rate sodium-ion batteries, Nano Energy 16 (2015) 389–398.

[21] D.W. Su, H.J. Ahn, G.X. Wang, SnO_2@graphene nanocomposites as anode materials for Na-ion batteries with superior electrochemical performance, Chem. Commun. 49 (2013) 3131–3133.

[22] J.F. Qian, Y. Xiong, Y.L. Cao, X.P. Ai, H.X. Yang, Synergistic Na-storage reactions in Sn_4P_3 as a high-capacity, cyclestable anode of Na-ion batteries, Nano Lett. 14 (2014) 1865–1869.

[23] W.J. Li, S.L. Chou, J.Z. Wang, J.H. Kim, H.K. Liu, S.X. Dou, $Sn_{4+x}P_3$@amorphous Sn-P composites as anodes for sodium-ion batteries with low cost, high capacity, long life, and superior rate capability, Adv. Mater 26 (2014) 4037, 4012.

[24] Y.C. Liu, N. Zhang, L.F. Jiao, J. Chen, Tin nanodots encapsulated in porous nitrogen-doped carbon nanofibers as a free-standing anode for advanced sodium-ion batteries, Adv. Mater. 27 (2015) 6702–6707.

[25] H.Y. Kang, Y.C. Liu, K.Z. Cao, Y. Zhao, L.F. Jiao, Y.J. Wang, H.T. Yuan, Update on anode materials for Na-ion batteries, J. Mater. Chem. A 3 (2015) 17899–17913.

[26] Z. Li, J. Ding, D. Mitlin, Tin and tin compounds for sodium ion battery anodes: phase transformations and performance, Acc. Chem. Res. 48 (2015) 1657–1665.

[27] W. Luo, F. Shen, C. Bommier, H.L. Zhu, X.L. Ji, L.B. Hu, Na-ion battery anodes: materials and electrochemistry, Acc. Chem. Res. 49 (2016) 231–240.

[28] Z. Hu, Z.Q. Zhu, F.Y. Cheng, K. Zhang, J.B. Wang, C.C. Chen, J. Chen, Pyrite FeS_2 for high-rate and long-life rechargeable sodium batteries, Energy Environ. Sci. 8 (2015) 1309–1316.

[29] Y.X. Wang, J.P. Yang, S.L. Chou, H.K. Liu, W.X. Zhang, D.Y. Zhao, S.X. Dou, Uniform yolk-shell iron sulfide–carbon nanospheres for superior sodium–iron sulfide batteries, Nat. Commun. 6 (2015) 8689.

[30] Z. Shadike, M.H. Cao, F. Ding, L. Sang, Z.W. Fu, Improved electrochemical performance of CoS_2–MWCNT nanocomposites for sodium-ion batteries, Chem. Commun. 51 (2015) 10486–10489.

[31] Y.N. Ko, Y.C. Kang, Co_9S_8–carbon composite as anode materials with improved Na-storage performance, Carbon 94 (2015) 85–90.

[32] Y.X. Wang, K.H. Seng, S.L. Chou, J.Z. Wang, Z.P. Guo, D. Wexler, H.K. Liu, S.X. Dou, Reversible sodium storage via conversion reaction of a MoS_2–C composite, Chem. Commun. 50 (2014) 10730–10733.

[33] S.H. Choi, Y.N. Ko, J.K. Lee, Y.C. Kang, 3D MoS_2–graphene microspheres consisting of multiple nanospheres with superior sodium ion storage properties, Adv. Funct. Mater. 25 (2015) 1780–1788.

[34] Y.Y. Lu, Q. Zhao, N. Zhang, K.X. Lei, F.J. Li, J. Chen, Facile spraying synthesis and high-performance sodium storage of mesoporous MoS_2/C microspheres, Adv. Funct. Mater. 26 (2016) 911–918.

[35] S.H. Choi, Y.C. Kang, Sodium ion storage properties of WS_2-decorated three-dimensional reduced graphene oxide microspheres, Nanoscale 7 (2015) 3965–3970.

[36] C.B. Zhu, P. Kopold, W.H. Li, P.A. van Aken, J. Maier, Y. Yu, Engineering nanostructured electrode materials for high performance sodium ion batteries: a case study of a 3D porous interconnected WS_2/C nanocomposite, J. Mater. Chem. A 3 (2015) 20487–20493.

[37] C.Q. Shang, S.M. Dong, S.L. Zhang, P. Hu, C.J. Zhang, G.L. Cui, A Ni_3S_2-PEDOT monolithic electrode for sodium batteries, Electrochem. Commun. 50 (2014) 24–27.

[38] W. Qin, T.Q. Chen, T. Lu, D.H.C. Chua, L.K. Pan, Layered nickel sulfide-reduced graphene oxide composites synthesized via microwave-assisted method as high performance anode materials of sodium-ion batteries, J. Power Sources 302 (2016) 202–209.

[39] S.P. Wu, R.Y. Ge, M.J. Lu, R. Xu, Z. Zhang, Graphene-based nano-materials for lithium–sulfur battery and sodium-ion battery, Nano Energy 15 (2015) 379–405.

[40] H.G. Wang, S. Yuan, D.L. Ma, X.B. Zhang, J.M. Yan, Electrospun materials for lithium and sodium rechargeable batteries: from structure evolution to electrochemical performance, Energy Environ. Sci. 8 (2015) 1660–1681.

[41] C.L. Yang, W.H. Li, Z.Z. Yang, L. Gu, Y. Yu, Nanoconfined antimony in sulfur and nitrogen co-doped three-dimensionally (3D) interconnected macroporous carbon for high-performance sodium-ion batteries, Nano Energy 18 (2015) 12–19.

[42] X.S. Song, X.F. Li, Z.M. Bai, B. Yan, D.J. Li, X.L. Sun, Morphology-dependent performance of nanostructured Ni3S2/Ni anode electrodes for high performance sodium ion batteries, Nano Energy 26 (2016) 533–540.

[43] G.Q. Wang, F.F. Tu, J. Xie, G.H. Du, S.C. Zhang, G.S. Cao, X.B. Zhao, High-performance Li–O_2 batteries with controlled Li_2O_2 growth in graphene/Au-nanoparticles/Au-nanosheets sandwich, Adv. Sci. 3 (2016) 1500339.

[44] J.W. Wang, X.H. Liu, S.X. Mao, J.Y. Huang, Microstructural evolution of tin nanoparticles during in situ sodium insertion and extraction, Nano Lett. 12 (2012) 5897–5902.

[45] Y. Liu, F.F. Fan, J.W. Wang, Y. Liu, H. Chen, K. Jungjohann, Y. Xu, Y. Zhu, D. Bigio, T. Zhu, C. Wang, In situ transmission electron microscopy study of electrochemical sodiation and potassiation of carbon nanofibers, Nano Lett. 14 (2014) 3445–3452.

[46] J. Wang, H. Luo, Y. Liu, Y. He, F. Fan, Z. Zhang, S. Mao, C. Wang, T. Zhu, Tuning the outward to inward swelling in lithiated silicon nanotubes via surface oxide coating, Nano Lett. 16 (2016) 5815–5822.

[47] J.W. Wang, X.H. Liu, S.X. Mao, J.Y. Huang, Microstructural evolution of tin nanoparticles during in situ sodium insertion and extraction, Nano Lett. 16 (2012) 5897–5902.

[48] Y.X. Yin, S. Xin, Y.G. Guo, L.J. Wan, Lithium-sulfur batteries: electrochemistry, materials, and prospects, Angew. Chem. Int. Ed. 52 (2013) 13186–13200.